SCIENCE CHINA
Chemistry

•ARTICLES•

February 2025 Vol.68 No.2: 733–744
https://doi.org/10.1007/s11426-024-2243-8

A low-cost wide bandgap polymer based on carboxylate substituted thiazole enables efficient organic solar cells with remarkable batch-to-batch reproducibility

Xiaodong Zhu[1†], Yuchen Lei[1†], Jianhong Gao[1*], Yanjun He[1], Jinsicheng Liu[1], Qian Guo[1], Xiang Gao[1], Liwei Xiong[1], Xunchang Wang[2], Renqiang Yang[2*] & Zhitian Liu[1*]

[1]*Hubei Engineering Technology Research Center of Optoelectronic and New Energy Materials, Hubei Key Laboratory of Plasma Chemistry and Advanced Materials, School of Materials Science and Engineering, Wuhan Institute of Technology, Wuhan 430205, China;*
[2]*Key Laboratory of Optoelectronic Chemical Materials and Devices (Ministry of Education), School of Optoelectronic Materials &Technology, Jianghan University, Wuhan 430056, China*

Received May 31, 2024; accepted August 8, 2024; published online October 17, 2024

Constructing the low-cost, high-efficiency, and good batch-to-batch reproducibility polymer donor is vitally important for the application of organic solar cells. Herein, we develop a structurally simple carboxylate-substituted thiazole as an electron-withdrawing building block to construct a low-cost polymer, PBTTzE, containing a facilely prepared chlorinated benzo[1,2-b:4,5-b′]dithiophene (BDTCl) donor unit. Benefiting from synergistic electron deficient effects of chlorination and ester group and C=N, as well as the noncovalent interaction of S···O and S···N, PBTTzE exhibits a deep HOMO energy level (−5.59 eV), and a planar skeleton structure. When combined with the IT-4F acceptor, the polymer (54 kDa) demonstrated a champion PCE of 15.87%, which is the highest value in the IT-4F-based binary devices to date. Moreover, PBTTzE exhibits excellent batch-to-batch reproducibility due to its very similar PCEs within a range of 43–76 kDa. In addition, an alloyed state and complementary absorption can be formed between PM6 and PBTTzE. Therefore, in a ternary device with PBTTzE added to the PM6:BTP-eC9 blend, a top PCE of 18.76% is achieved due to the suppressed energy loss, prolonged exciton diffusion distance, and improved charge transport. Our work demonstrates that the carboxylate-substituted thiazole is a highly promising acceptor unit for constructing low-cost and high-performance polymers.

carboxylate substituted thiazole, polymer donor, low-cost, batch-to-batch reproducibility, organic solar cells

Citation: Zhu X, Lei Y, Gao J, He Y, Liu J, Guo Q, Gao X, Xiong L, Wang X, Yang R, Liu Z. A low-cost wide bandgap polymer based on carboxylate substituted thiazole enables efficient organic solar cells with remarkable batch-to-batch reproducibility. *Sci China Chem*, 2025, 68: 733–744, https://doi.org/10.1007/s11426-024-2243-8

1 Introduction

As a new generation of solar energy harvesting technology, bulk heterojunction (BHJ) organic solar cells (OSCs) have obtained increasing interest and have been extensively explored because of various unparalleled advantages of easy fabrication, light weight, low-cost solution processing, flexibility, colored and semitransparency [1–4]. Interestingly, these features endow the device new applications in the fields of wearable device, integrated building, greenhouse agriculture, etc., increasing its market competitiveness [5–7]. Attributed to material innovation, device engineering, and multi-component strategy, especially the emergence of representative non-fullerene acceptors (NFAs) ITIC [8] and Y6 [9], the impressive power conversion efficiency (PCE) of

†These authors contributed equally to this work.
*Corresponding authors (email: gaojianhong26@wit.edu.cn; able.ztliu@wit.edu.cn; yangrq@jhun.edu.cn)

state-of-the-art devices have achieved over 19% for single-junction and 20% for tandem structures [10–17], reaching the level of commercial applications.

Considering the commercial applications of OSCs, low cost is the most important factor to be considered without sacrificing the photovoltaic performance. Currently, almost all of the OSCs with record performance are based on wide bandgap donor-acceptor (D-A) type conjugated polymer donors and narrow bandgap fused ring small molecule acceptors [18–23]. However, these materials have complicated molecular structures, resulting in multi-step synthesis and high cost. Therefore, it is very important to design and synthesize high-efficiency and low-cost active layer materials to meet the practical applications of OSCs. Inspiringly, the development of partially or fully non-fused small molecules can significantly reduce synthesis costs. Meanwhile, these molecules can still keep the better planar geometry of the π-conjugated skeleton by constructing the noncovalent intramolecular interactions to lock the molecular configuration [24–32]. And recent reports also verified that the non-fused acceptors were able to achieve over 17% efficiency [33]. For polymers, P3HT is an excellent donor candidate for low-cost module fabrications, but its poor PCE limits its application [34,35]. Therefore, high-performance NFA-based OSCs so far have been fabricated using the D-A polymer donors, which is mainly due to the intramolecular electron push-pull effects between D and A units affording the polymers downshifted molecular energy levels and enhanced π-π stacking [36]. However, the complicated synthetic routes and high costs of these representative polymers, such as PBDB-T, PM6, D18, and J52, are adverse to the widespread commercial applications of OSCs [37–42]. Recently, continuous endeavors have been expended to develop high-performance polymers with relatively short synthetic procedures (including PTQ-10, PTQ12-5, PBCT-2F, PB2, PBTTz3Cl, and X1), and some can match well with various NFAs to achieve elevated PCEs [43–48]. However, compared with the booming growth of NFAs, the species of high-performance polymer donors used to pair with NFAs are still limited. Therefore, it is urgent to design and synthesize polymer donors with simple structure and high efficiency, which should match well with various NFAs for the development and application of OSCs. Additionally, it is worth noting that the molecular weight (M_n) of polymers should be meticulously regulated owing to its effect on solubility, aggregation, crystallinity, molecular orientation, charge mobilities, and recombination, as well as final PCE [49–53]. Generally, conjugated polymers with high M_n are conducive to improve device performance. However, excessive enlarged M_n causes reduced solubility and increased aggregation, resulting in large phase separation size and poor device performance [54]. In addition, M_n variation is often considered as the main reason for batch-to-batch variations [10,44,45]. Therefore, ideal polymer donors of OSCs should have a simple molecular structure to reduce synthetic cost, a moderate molecular weight to improve phase separation, complementary absorption spectra with NFAs to ensure high short-circuit current (J_{sc}), a deep highest occupied molecular orbital (HOMO) energy level to guarantee low energy loss and high open-circuit voltage (V_{oc}), and suitable aggregation behavior to form preferential self-assembly into a fibril nanostructure.

Among the typical polymers, the benzo [1,2-b:4,5-b′] dithiophene (BDT) unit is widely applied as an excellent D building block to construct conjugated polymers due to its relatively large planar conjugated, electron-rich effect, and small steric hindrance [55,56]. These features endow the polymer high charge carrier mobility, suitable energy level distribution, favorable crystallinity and orientation, thus contributing to satisfactory efficiency. In particular, the halogen atoms, e.g. fluorine and chlorine, were introduced into the thiophene of the BDT unit to fine-tune the energy levels and aggregation properties [57]. In contrast, chlorination BDT unit can provide extensive application prospects due to its relatively short synthesis procedures [45]. Therefore, compared to the mainstream polymers (A units of PM6 and D18 require 6 steps and 8 steps, respectively) [44], it is of vital importance to develop the simple acceptor (A) units to build high-efficiency and low-cost polymer donors. In this work, thiazole was selected as an A unit to construct wide bandgap polymers because of its weak electron withdrawing ability and coplanar structure [58]. Moreover, introduction of an ester group at the 4-position of the thiazole (4ETz) unit can not only improve the solubility but also further strengthen the electron-accepting ability, which is beneficial for down-shifting HOMO energy level. Meanwhile, esterified *N*-heteroatom can also effectively maintain molecular planarity due to the formation of noncovalent N···S and S···O interaction. More importantly, the 4ETz can also be facilely prepared from commercially available materials.

Hence, a novel donor polymer, named PBTTzE, was synthesized with low-cost 4ETz as the A unit, in combination with a facilely prepared chlorinated BDT donor unit (Figure 1). Remarkably, PBTTzE with a simple molecular structure, displays a high absorption coefficient at 534 nm and a wide band gap of 2.01 eV. Benefiting from the synergistic electron deficient effects of both Cl and ester group, PBTTzE exhibits low-lying HOMO energy level of −5.59 eV, which is beneficial to obtain a high V_{oc}. Additionally, chlorinated can also effectively regulate the aggregation behavior of PBTTzE. The noncovalent interactions induced by the N and O atoms of 4ETz are conducive to planar molecular skeleton and charge-carrier delocalization. Furthermore, we investigated the effect of M_n of PBTTzE on blend morphology and photovoltaic performance. Among them, the blend film fabricated with medium M_n (54 kDa)

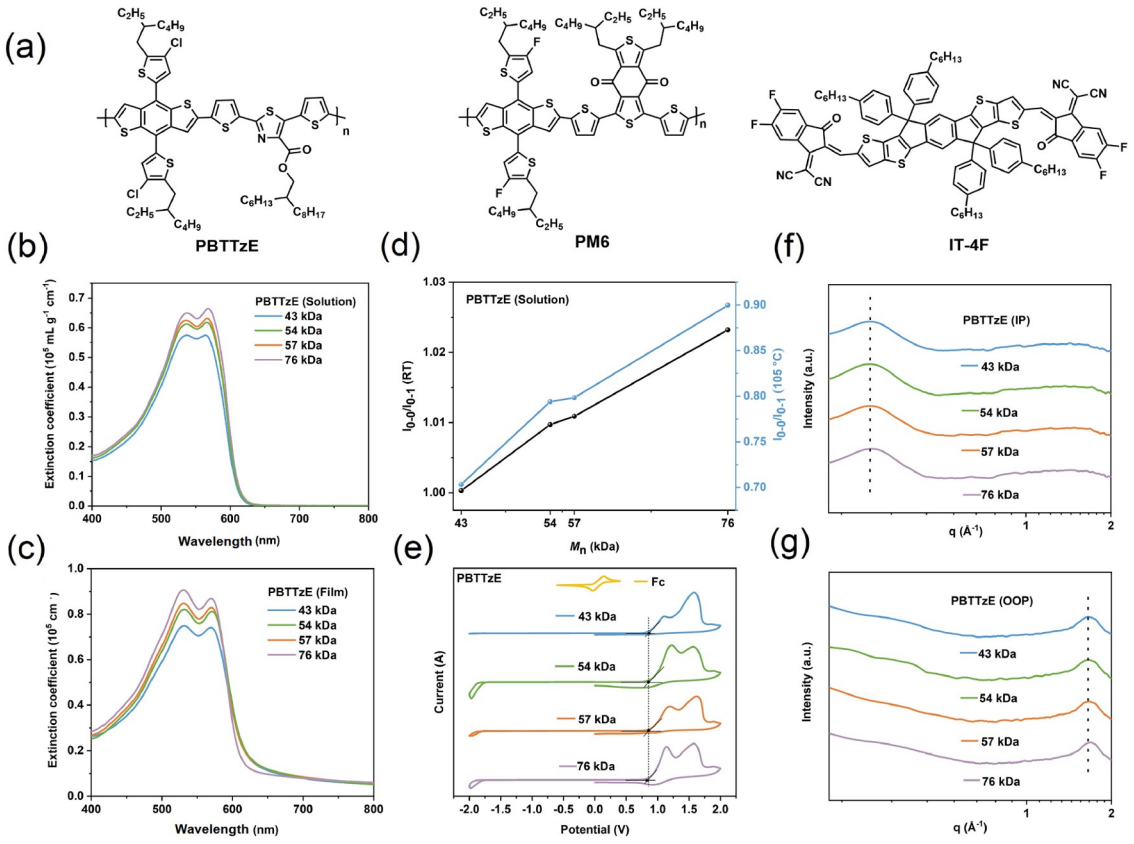

Figure 1 (Color online) (a) Chemical structures of PBTTzE, PM6 and IT-4F; (b,c) UV-vis absorption spectra of polymers in solution and in film; (d) The intensity ratio of main absorption peak and shoulder peak at different temperatures; (e) Cyclic voltammetry curves of PBTTzEs, and the Fc/Fc^+ redox couple is used as the reference; GIWAXS line-cut profiles of pure films in (f) IP and (g) OOP directions.

displays improved phase separation, reduced π-π stacking distance and enhanced crystal coherence length (CCL) value. Finally, a maximum PCE of 15.87% was achieved in device, which is the highest PCE for IT-4F-based binary OSCs so far. Interestingly, the four batches of PBTTzE with M_ns ranging from 43 to 76 kDa showed very similar PCEs, suggesting that the PBTTzE possesses excellent batch-to-batch reproducibility. In addition, a small amount of PBTTzE (10 wt%) was introducted into the PM6:BTP-eC9 host blend, affording increased photon utilization at the short wavelength, reduced energy loss, and optimized morphology, thus producing a top PCE of 18.76% for ternary blend device.

2 Results and discussion

2.1 Synthesis and characterizations of PBTTzE

The chemical structures of PBTTzE, PM6 and IT-4F are shown in Figure 1a, where the synthetic route and detailed procedures of PBTTzE are depicted in Scheme S1 (Supporting Information online). The starting material of methyl 2,5-dibromothiazole-4-carboxylate is commercially available, and was then copolymerized with 2-(tributylstannyl) thiophene via a Pd-catalyzed Stille coupling to form compound **1**. Subsequently, compound **2** was obtained from alkylation reaction, and followed by bromination to give monomer TTzE-Br. After just three-stepped common reactions, the target monomer could be obtained with a very high overall yield of over 60%, which is a key factor for cutting material costs. Finally, the polymer PBTTzE was prepared by Stille coupling polymerization between the TTzE-Br and the commercially available donor unit of (4,8-bis(4-chloro-5-(2-ethylhexyl)thiophen-2-yl)benzo[1,2-b:4,5-b′]dithiophene-2,6-diyl)bis (trimethylstannane). All compounds were purified by silica gel column chromatography, and their structures and purity were verified by ^{1}H nuclear magnetic resonance spectroscopy (NMR), ^{13}C NMR, and electron impact mass spectrometry (EIMS), and the corresponding spectra are shown in Figure S1–S9 (Supporting Information online). To better understand the advantage of PBTTzE, the costs of PBTTzE and some representative polymers were evaluated according to the industrial figure of merit (i-FOM) [59–61]. The detailed analysis data are listed in Table S1 [62–69]. The results found that PBTTzE possesses a lower synthetic complexity (SC) and a higher FOM than other polymers with PCEs over 13% based on IT-4F. Therefore, it

would be an easily available and large-scale manufacturable donor material from a commercialization perspective. In addition, PBTTzE with various M_ns was synthesized by changing the solvent type, polymerization temperature and reaction time. The corresponding number average molecular weights of four batches of PBTTzE measured by high-temperature gel-permeation chromograph (GPC) using 1,2,4-trichlorobenzene as eluent are 43, 54, 57 and 76 kDa with polydispersity indexes of 2.3, 2.4, 2.0, and 2.3, respectively (Figure S10). Of note that the solubility of PBTTzEs slightly decreased with the increased M_n, they can still be dissolved in general solvents, including chloroform, chlorobenzene, and *o*-dichlorobenzene. Meanwhile, thermal properties of polymers were determined by thermogravimetric analysis (TGA). The corresponding detailed information can be found in Figure S11 and Table 1. All the PBTTzE samples exhibit excellent thermal stability with a weight loss temperature (5%) up to 370 °C. This suggests that the different M_ns have little influence on the thermal stability of polymers.

The optical properties of polymers in chlorobenzene solutions and in films were investigated by ultraviolet-visible (UV-vis) absorption spectra, and the results are shown in Figure 1b,c and Table 1. In solution, all polymers display almost identical absorption profile in the range of 400–650 nm with the main absorption peak (0-1) and shoulder peak (0-0) of ~536 nm and ~566 nm, respectively. However, both featured peaks gradually enhanced with the increase of M_n. Obviously, the intensity ratio of $I_{0\text{-}0}/I_{0\text{-}1}$ with the largest M_n of 76 kDa (1.02) is slightly higher, while the $I_{0\text{-}0}/I_{0\text{-}1}$ values of 43, 54, and 57 kDa are 1.00, 1.01, and 1.01, respectively (Figure 1d). This result confirmed that enhancement of the intermolecular interactions and aggregation properties can be improved by optimizing M_n. Furthermore, the temperature-dependent absorption spectra were measured in chlorobenzene solutions to investigate aggregation behaviors of polymers (Figure S12). The four batches of polymer still show a shoulder peak even when the temperature rises to 105 °C, implying the strong aggregation abilities in solution. Such a characteristic is close association with a highly planar structure PBTTzE, which is obtained due to formation of noncovalent S···O and S···N interactions, as evidenced by the density functional theory (DFT) calculation (Figure S13). In PBTTzE, the distances are 3.06 Å between S and N and 3.14 Å between S and O, which are shorter than their sum of van der Waals radii of 3.35 Å for S (1.80 Å) and N (1.55 Å), and 3.32 Å for S and O (1.52 Å) , respectively, indicating significant noncovalent S···O and S···N interactions. In addition, the polymer with the highest M_n (76 kDa) exhibits the strongest intensity ratio of $I_{0\text{-}0}/I_{0\text{-}1}$ of 0.90 at 105 °C (Figure 1d), which may lead to a weak compatibility with IT-4F. As for the thin film, the absorption spectra of PBTTzE with various M_n display a slightly red-shift compared with solution state. Moreover, the absorption coefficients are also increased along with the M_n increasing, which is likely a result of more ordered stacking and denser film for high M_n PBTTzE. This characteristic benefits light harvesting to obtain a higher short circuit current density (J_{sc}). The optical bandgaps (E_g^{opt}) are 2.01 eV for all polymers based on absorption onset at 617 nm, indicating that the effective conjugation length of the polymer main chain is nearly saturated in the range of 43–76 kDa [70].

The energy levels of PBTTzE with different M_n were determined by cyclic voltammetry (CV), and the corresponding energy level diagram is illustrated in Figure 1e. On the basis of the onset of oxidation potential, the highest occupied molecular orbital (HOMO) energy levels of polymers were determined to locate at −5.60, −5.59, −5.59, and −5.58 eV, respectively. However, no obvious reduction potential could be observed. Therefore, the lowest unoccupied molecular orbital (LUMO) energy levels of 43, 54, 57, and 76 kDa were approximately calculated as −3.59, −3.58, −3.58, and −3.57 eV, respectively, according to the Eq. (1):

$$E_{LUMO} = E_{HOMO} + E_g^{opt} \quad (1)$$

The almost identical energy level distributions can be observed from 43 to 54 and 57 kDa. However, a slightly increased trend is found for 76 kDa. Because of synergetic effect of strong electronegativity, they all show the deeper HOMO level, which are beneficial to obtain higher V_{oc} in OSCs. Meanwhile, diminishing the HOMO level differences (ΔE_{HOMO}) between the polymer and IT-4F may also affect the charge transport process, and thus influence the photocurrent.

Table 1 Molecular weight, optical properties, bandgaps, and thermogravimetric of the four polymers with different molecular weights

PBTTzE [a] M_n [kDa]	PDI	λ_{sol} [b] [nm]	$\lambda_{sol,\ 105\ °C}$ [b] [nm]	λ_{film} [b] [nm]	$I_{0\text{-}0}/I_{0\text{-}1}$ [c] [Sol, RT]	$I_{0\text{-}0}/I_{0\text{-}1}$ [c] [Sol, 105 °C]	E_g^{opt} [d] [eV]	T_g [e] [°C]
43	2.3	536, 564	513, 553	535, 573	1.00	0.70	2.01	370
54	2.4	536, 566	517, 554	534, 573	1.01	0.79	2.01	374
57	2.0	536, 567	518, 554	533, 573	1.01	0.80	2.01	376
76	2.3	537, 568	521, 555	533, 573	1.02	0.90	2.01	377

a) Determined by high temperature GPC; b) Determined by the UV-vis spectra of solution and film from the chlorobenzene solution; c) The intensity ratio of main absorption peak (0-1) and shoulder peak (0-0); d) Calculated from the absorption edge of the polymer films: $E_g^{opt} = 1240/\lambda_{edge}$; e) Determined by thermogravimetric analysis.

The grazing incidence wide angle X-ray scattering (GIWAXS) was performed to investigate the effect of M_n on molecular packing and orientation in neat films. As depicted in Figure 1f,g and Figure S14, all films exhibit a preferential face-on orientation with representative π-π stacking peak (010) in the out-of-plane (OOP) direction and lamellar peak (100) in-plane (IP) direction, indicating that the molecular orientation is almost unaffected. However, the gradually narrowed angular distribution is observed in the (010) diffraction peak with increasing M_n, suggesting the enhanced molecular crystalline. Subsequently, we used the Scherrer equation to determine the CCL value of the π-π stacking peak. As is shown in Table S2, the CCL values were calculated to be 24.57, 24.57, 26.91, and 28.26 Å for PBTTzE films based on 43, 54, 57, and 76 kDa, respectively. It is obvious that the 76 kDa possesses the stronger crystallization ability compared to others. Moreover, the highest M_n shows the smallest π-π stacking distance, demonstrating the strongest intermolecular aggregation, which is consistent with the largest intensity of $I_{0\text{-}0}/I_{0\text{-}1}$ in the absorption spectrum as mentioned above. The results conclude that M_n has a great influence on the stacking distance and crystallization behavior, thereby impacting the active layer morphology, charge transport property and photovoltaic performance.

2.2 Photovoltaic properties

In order to investigate the influence of PBTTzEs on the photovoltaic performances, the OSCs with a conventional device structure of ITO/PEDOT:PSS/Active layer/PDINN/Ag were fabricated and characterized. The detailed device optimization process, such as donor and acceptor (D/A) weight ratio, film thickness, additive content, and thermal annealing temperature, are listed in Table S3. Figure 2a exhibits the current density-voltage (*J*-*V*) curves of the optimized OSCs with the same D/A weight ratio of 1:1 for all devices and 0.75 vol% DIO as additive, and thermal annealing at 100 °C for 10 min. The photovoltaic parameters of the corresponding best-performing devices are summarized in Table 2. Obviously, an excellent efficiency of 15.87% is obtained for 54 kDa PBTTzE-based device with an open-circuit voltage (V_{oc}) of 0.891 V, a short-circuit current density (J_{sc}) of 23.13 mA cm^{-2}, and a fill factor (FF) of 0.769. This device efficiency is the highest value reported to date for the IT-4F-based OSCs (Figure 2c).

In contrast, the device based on the smallest M_n (43 kDa) shows a relatively low efficiency of 14.91%, due to decreased J_{sc} and FF. Interestingly, the efficiency is almost identical between 54 kDa and 57 kDa PBTTzE-based devices, which is in accordance with the characteristics of pure films discussed above. When the molecular weight further increases to 76 kDa, a slightly lower performance of about 15.27% is found with reduced J_{sc}. However, a higher V_{oc} could be obtained for 76 kDa, which is mainly attributed to the extended quasi-Fermi levels between electrons and holes upon decreased charge carrier mobility [71]. As a result, the V_{oc} of organic solar cells not only depends on the electronic levels of the donor and acceptor, but critically depends on charge dynamic. Importantly, given the large range of variation in M_n (43–76 kDa), only 1% difference in device

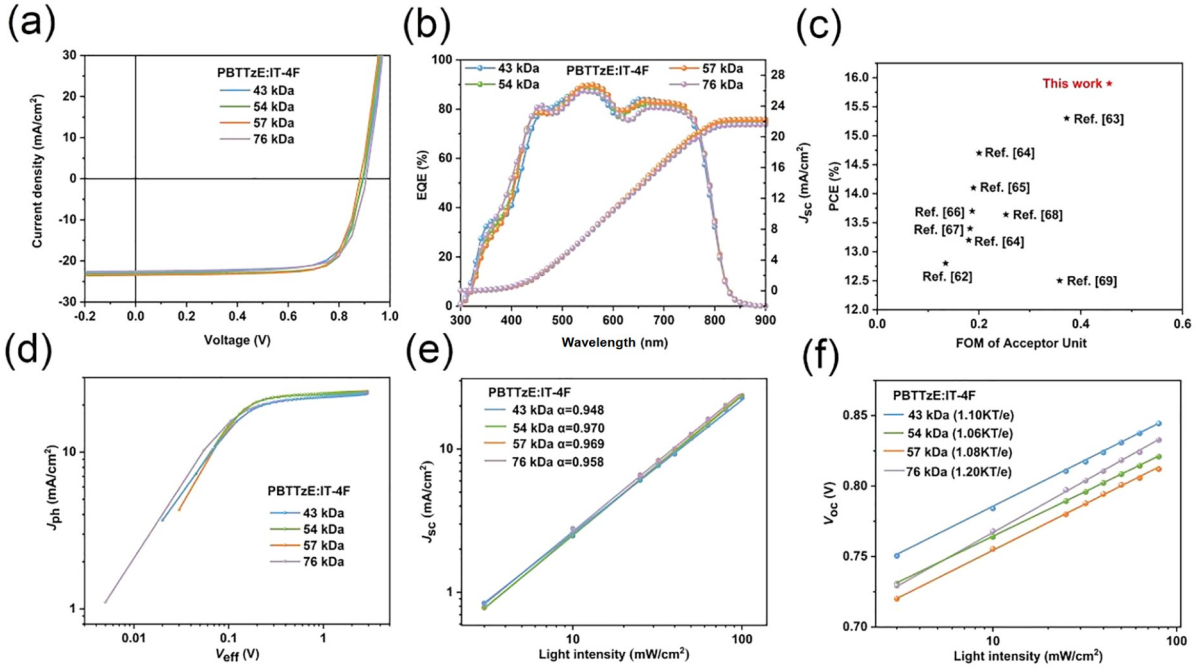

Figure 2 (Color online) (a) Optimized *J*-*V* curves and (b) EQE spectrum of PBTTzE:IT-4F devices with different molecular weights. (c) Cost-Efficiency diagram based on receptor IT-4F. The light intensity dependence profiles with (d) J_{ph}-V_{eff} and (e, f) J_{sc} and V_{oc} curves of the devices.

performance means that the PBTTzE possesses excellent batch-to-batch reproducibility. The J_{sc} differences for all devices are confirmed by the external quantum efficiency (EQE) measurements. As shown in Figure 2b, all polymers show broad spectral response in the range of 300–900 nm, and the devices of 54 kDa and 57 kDa exhibit the maximum EQE, which can be attributed to high absorption ability. However, the 76 kDa PBTTzE-based device with the strongest absorption coefficient did not achieve the expected EQE. Moreover, there is an obvious contrast between FF and increasing M_n. The results prompted us to find further supporting evidence by investigating the film morphology. Ultimately, the integrated J_{sc} values calculated from the EQE are highly matched with the *J*-*V* tests.

2.3 Morphology properties

To further explore the effect of M_n on device performances, atomic force microscopy (AFM) and transmission electron microscopy (TEM) were used to investigate the blend film morphology. As seen in Figure 3a–d, the blend film of 43 kDa shows a relatively smooth surface with the smallest root-mean-square (RMS) roughness of 1.68 nm among the four batches, while that of 76 kDa exhibits the biggest RMS of 6.23 nm with serious phase separation and large aggregated domain (Figure S15). In contrast, both 54 kDa and 57 kDa PBTTzE-based blend films display the more moderate phase separation and clearer fiber distribution, which would be more favorable for exciton dissociation and charge transport, and then significantly increase the J_{sc} and FF values. To a certain extent, the miscibility between donor and acceptor materials affects the degree of phase separation of blend films. Therefore, we further measured the contact angles by using deionized water and glycerol to analyze the surface energy of PBTTzEs and IT-4F films (Figure S16). The miscibility can be evaluated using the Flory-Huggins interaction parameters (χ), which is obtained by an experimental Eq. (2):

$$\chi = K\left(\sqrt{\gamma_D} - \sqrt{\gamma_A}\right)^2 \quad (2)$$

where K is a constant, γ_D and γ_A are the surface tension of PBTTzEs and IT-4F, respectively. As shown in Table S4, the χ values, between polymers and IT-4F, exhibit an increasing tendency with increasing M_n. The largest χ value of 0.69 for PBTTzE with 76 kDa and IT-4F film means the lowest miscibility of two phases, leading to the increased phase segregation. This result is consistent with the AFM and TEM analysis with the large RMS value and aggregated domain in

Table 2 Photovoltaic device parameters of the OSCs based on PBTTzE:IT-4F with various polymer molecular weights under AM 1.5 G illumination, 100 mW cm^{-2}

Devices	Thickness [nm]	V_{oc} [V]	J_{sc} [mA cm^{-2}]	J_{calc} [a)] [mA cm^{-2}]	FF	PCE$_{max\ (avg)}$ [b)] [%]
PBTTzE (43 KDa):IT-4F	100	0.894	22.79	21.87	0.731	14.91 (14.76 ± 0.15)
PBTTzE (54 KDa):IT-4F	104	0.891	23.13	21.98	0.769	15.87 (15.76 ± 0.11)
PBTTzE (57 KDa):IT-4F	104	0.881	23.43	22.26	0.761	15.72 (15.63 ± 0.09)
PBTTzE (76 KDa):IT-4F	109	0.906	22.46	21.57	0.751	15.27 (15.22 ± 0.05)

a) Integrated from EQE spectrum; b) average values were obtained from 15 devices.

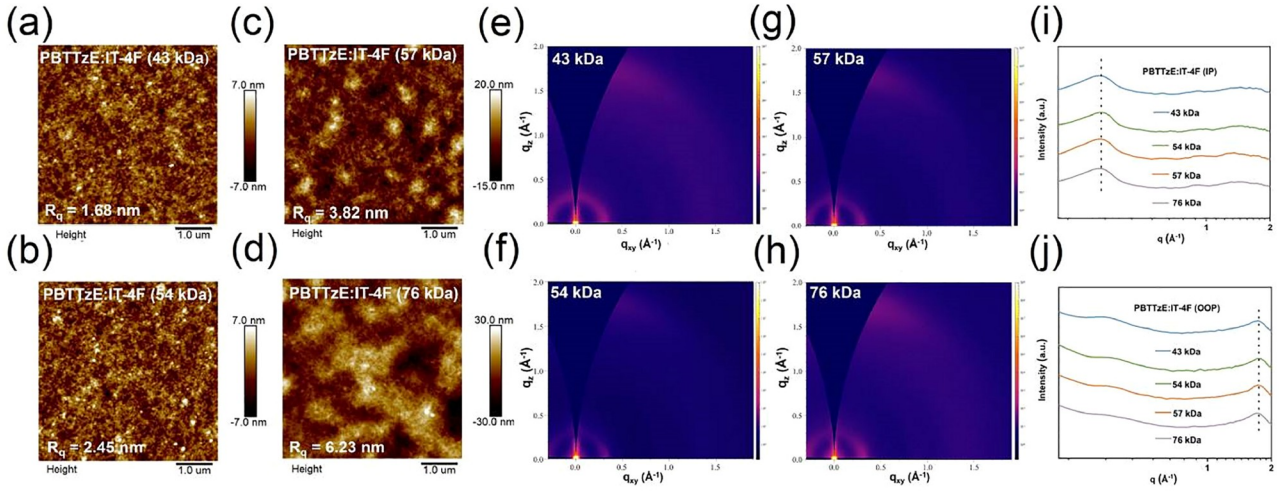

Figure 3 (Color online) (a–d) AFM height images; (e–h) 2D-GIWAXS patterns and (i, j) corresponding 1D line-cut profiles for PBTTzE:IT-4F blend films with different polymer molecular weights.

the PBTTzE (76 kDa):IT-4F blend film.

GIWAXS analysis was carried out to understand the molecular packing and orientation of the blend films. As shown in Figure S17, the pristine IT-4F film adopts an intermixed edge-on/face-on orientation due to the simultaneous appearance of (100) lamellar diffraction and (010) π-π stacking peaks along with IP and OOP directions, respectively. When blended with the PBTTzEs, all blend films exhibit a strong (010) diffraction peak at ~1.74 $Å^{-1}$ in the OOP direction and a strong (100) diffraction peak at ~0.31 $Å^{-1}$ in the IP direction (Figure 3e–j), indicating a comparable prominent face-on orientation and more ordered molecular packing. Meanwhile, we also observed a weak (100) diffraction peak at 0.35 $Å^{-1}$ in the OOP direction while no obvious (010) crystalline region could be observed at 1.53 $Å^{-1}$ in IP direction, suggesting the diffraction peaks in the blend films are mainly from the polymers. Additionally, diminished intensity and distance of the lamellar packing and π-π stacking peaks in blend films compared to the pure films (Figure 1f,g) are attributed to the differentiated donor/acceptor intermolecular interactions, thus influencing their morphological characteristics. Moreover, the calculated π-π stacking distances for 43, 54, 57, and 76 kDa blend films show 3.61, 3.59, 3.61 and 3.67 Å with CCL values of 18.84, 22.61, 21.74 and 20.19 Å (Table S5), respectively. Remarkably, the smaller π-π stacking distance and larger CCL of the PBTTzE (54 kDa):IT-4F blend tend to form better charge transport and collection, thus explaining the improved J_{sc} and FF.

2.4 Charge dissociation, recombination, and transport

The analysis of charge dissociation, recombination, and transport behaviors is beneficial to better understand the difference in the J_{sc} and FF of four batch devices. Firstly, the exciton dissociation probabilities ($P_{diss} = J_{ph}/J_{sat}$, where J_{sat} is the saturation current density) were investigated by using photocurrent density (J_{ph}) versus effective voltage (V_{eff}) curves (Figure 2d). Under short-current conditions, the P_{diss} was determined to be 95.9%, 96.3%, 96.1%, and 94.8% for devices based on PBTTzE with 43, 54, 57 and 76 kDa, respectively, suggesting that moderate M_ns (54 kDa and 57 kDa) are more beneficial to exciton dissociation. However, the reduced P_{diss} of PBTTzE (76 kDa):IT-4F is one of the reasons for its lowest J_{sc}. Next, we explored the charge recombination processes by examining the *J-V* curve responding to gradually increased incident light intensity (P_{light}), and the results are shown in Figure 2e,f. According to the formular $J_{sc} \propto P_{light}^{\alpha}$, the calculated α values of 54 kDa (0.970) and 57 kDa (0.969) of PBTTzE-based devices are closer to 1 than those of other two devices (0.948 for 43 kDa and 0.958 for 76 kDa), meaning that the bimolecular recombination is suppressed. Meanwhile, measurement of V_{oc} as a function of P_{light} was carried out to probe monomolecular recombination within the devices. The curves were fitted according to the expression $V_{oc} \propto (nk_BT/q)\ln(P_{light})$, where the slope close to k_BT/q implies that monomolecular recombination is restrained. The slopes of 43, 54, and 57 kDa PBTTzE based devices were calculated to be 1.10, 1.06, and 1.08 k_BT/q, respectively, indicating that the M_ns have slight influence on the monomolecular recombination in the range of 43–57 kDa. Nevertheless, there is more monomolecular recombination in device fabricated by 76 kDa (1.20 k_BT/q), which is attributed to more serious phase separation as verified above. Furthermore, the charge transport properties were analyzed by applying space charge limited current (SCLC) method to investigate hole mobilities (μ_h) and electron motilities (μ_e). As shown in Figure S18, the μ_h and μ_e values are $3.41\times10^{-4}/2.51\times10^{-4}$ $cm^2\ V^{-1}\ s^{-1}$, $5.89\times10^{-4}/5.46\times10^{-4}$ $cm^2\ V^{-1}\ s^{-1}$, $5.67\times10^{-4}/5.03\times10^{-4}$ $cm^2\ V^{-1}\ s^{-1}$ and $5.37\times10^{-4}/4.30\times10^{-4}$ $cm^2\ V^{-1}\ s^{-1}$ for the 43, 54, 57, and 76 kDa of PBTTzE-based devices, with a μ_h/μ_e ratio of 1.36, 1.08, 1.13, and 1.25, respectively. Apparently, balanced and high carrier mobilities in 54 kDa devices are favorable for charge transport, simultaneously, combined with suppressed charge recombination and effective exciton dissociation, thus obtaining the best J_{sc} and FF. These results also demonstrate that turning the M_n strategy can be used to optimize the physical characterization and morphology of materials, further improving the device performance.

2.5 Ternary organic solar cells

Benefiting from broadening the absorption range, turning the energy level alignment and optimizing the morphology of the active layer, the ternary strategy has proven to be a simple and effective method to further improve device performance. Interestingly, compared to PM6, PBTTzE exhibits a certain degree of blue-shifted and strong aggregation ability (Figure 4a), which contributes to the formation of complementary absorption in the short wavelength region and regulate the film morphology to improve J_{sc}. Meanwhile, a cascade HOMO energy alignment is formed between PBTTzE (−5.59 eV), PM6 (−5.50 eV), and BTP-eC9 (−5.63 eV), as shown in Figure 4b, which is conducive to hole transport. Furthermore, contact angle measurements showed that the χ value of PM6:PBTTzE is 0.0018, which is smaller than 0.14 of PM6:BTP-eC9 and 0.26 of PBTTzE:BTP-eC9 (Figure S19 and Table S6), indicating better miscibility between PM6 and PBTTzE, thus tending to form a donor alloy [72]. Also, we found that the HOMO energy level of the PM6:PBTTzE blend gradually declined with the increase of PBTTzE content (Figure 4c), which further confirmed that PM6 and PBTTzE can form an alloy state. Therefore, introduction of PBTTzE into the binary blend can effectively regulate the energy level and E_{loss}, leading to a significantly increased V_{oc}.

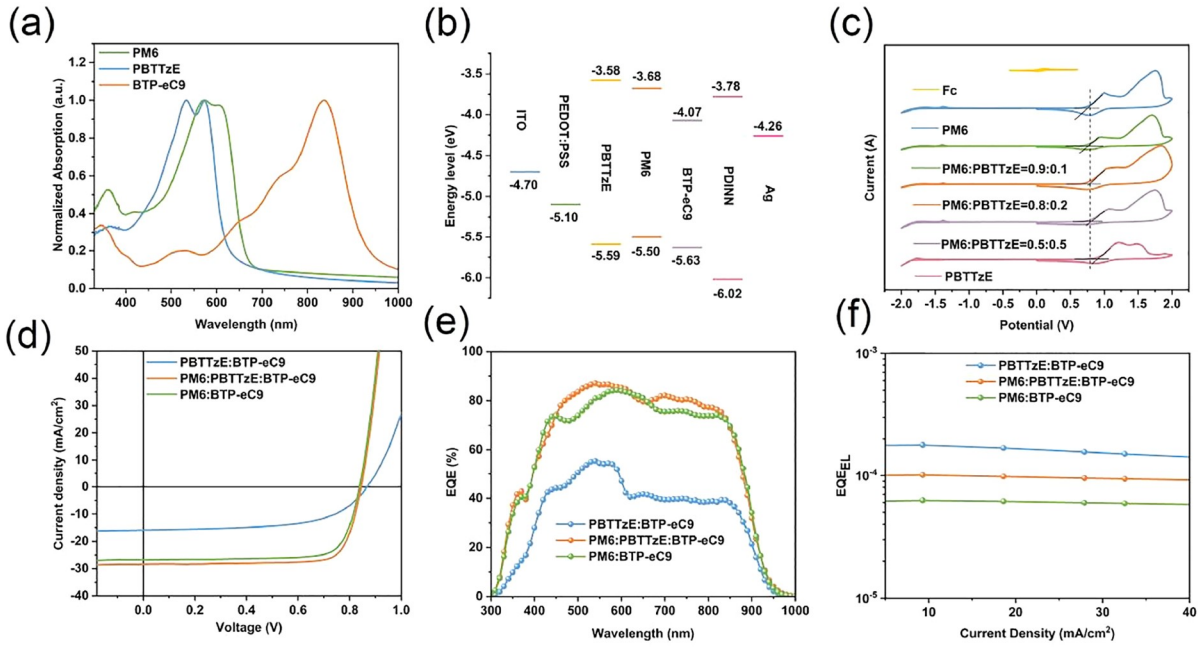

Figure 4 (Color online) (a) Normalized absorption spectra of neat polymer donors and BTP-eC9 films. (b) The energy level alignment of the electrode, interface layer and photovoltaic materials. (c) Cyclic voltammetry curves of PM6:PBTTzE blend with various PBTTzE contents. (d) *J*–*V* characteristics, (e) EQE spectra, and (f) EQE_{EL} curves of the binary and optimized ternary devices.

Based on these features, the ternary device was prepared by inserting PBTTzE (54 kDa) as a donor guest into the binary system based on PM6:BTP-eC9. A conventional device architecture of ITO/PEDOT:PSS/active layer/PDINN/Ag was used to investigate the photovoltaic performance for PM6 and PBTTzE based binary and ternary OSCs. The donor/acceptor (D/A) weight ratio was kept constant (1:1.2). The corresponding *J*-*V* curves are shown in Figure 4d, and the detailed photovoltaic parameters were summarized in Table 3 and Table S7. The representation device of PM6:BTP-eC9 shows an excellent PCE of 17.26% along with a J_{sc} of 27.01 mA cm^{-2}, a V_{oc} of 0.839 V, and an FF of 0.761, while the PCE of PBTTzE:BTP-eC9 device is only 10.45% with relatively lower J_{sc} (17.86 mA cm^{-2}) and FF (0.675) but higher V_{oc} (0.866 V). Interestingly, an improved PCE of 18.76% with excellently improved J_{sc} (28.38 mA cm^{-2}) and FF (0.782) and slightly elevated V_{oc} was obtained when PBTTzE was introduced into a binary system with the weight ratio of 0.9:0.1:1.2 (PM6:PBTTzE:BTP-eC9). The improved J_{sc} can be explained by the increased EQE value in comparison to the reference device (Figure 4e), which is consistent with the absorption spectra of blend films with extended absorption range at 450–600 nm and increased absorption coefficient at 750–800 nm (Figure S20). Moreover, the deviations of J_{sc} between the testing and calculated from integration of the EQE spectra are within a 5% range. Of note is that the improvement in V_{oc} for ternary OSC probably results from the low energy loss (E_{loss}). Therefore, we explored the E_{loss} of optimized binary and ternary devices by testing the highly sensitive external quantum efficiency (s-EQE) and electroluminescent (EL). The detailed E_{loss} can be divided into three parts based on the SQ limit [73], as follows:

$$\begin{aligned} E_{loss} &= E_g - qV_{oc} \\ &= (E_g - qV_{oc}^{SQ}) + (qV_{oc}^{SQ} - qV_{oc}^{rad}) + (qV_{oc}^{rad} - qV_{oc}) \\ &= \Delta E_1 + \Delta E_2 + \Delta E_3 \end{aligned} \quad (3)$$

where E_g could be estimated according to the crossing point between the normalized absorption and emission spectra of the blend films (Figure S21). As shown in Figure 4f, the ΔE_3 was also calculated by directly measuring the external quantum efficiency of electroluminescence (EQE_{EL}) of the solar cell through Eq. (4):

$$\Delta E_3 = -kT\ln(EQE_{EL}) \quad (4)$$

The calculated values are shown in Table 3. It is pretty much the same of ΔE_1 for the optimal binary and ternary devices. The differences in E_{loss} for all blend films should be mainly due to the changes in ΔE_2 and ΔE_3. Apparently, the optimized ternary device had lower E_{loss} than the PM6:BTP-eC9-based counterpart, and thus achieved a higher V_{oc}. This result also demonstrated that the alloyed state of PM6:PBTTzE in the ternary device can effectively reduce the HOMO energy level. However, there is also a diminished offset between donor and acceptor.

In general, reducing the offset in the OSCs may affect the exciton dissociation due to a lower driving force. However, enhancement of J_{sc} could be formed when adding 10 wt% PBTTzE into PM6:BTP-eC9 system. Therefore, a series of photophysical characterizations were investigated to analyze

the reasons for the efficiency improvement. The photogenerated exciton separation dynamics of three blends were first investigated using the transient absorption spectroscopy (TAS) technique. An excitation wavelength at 780 nm was used to excite the acceptor (BTP-eC9) to study the hole transfer processes because of decreased HOMO offset between alloy donor and BTP-eC9. The TAS images and corresponding decay dynamics are shown in Figure 5a–e and Figure S22. The ground state bleaching (GSB) signal of BTP-eC9 lies at 610–860 nm, and with the decay of TAS signals from the acceptor, the new bleaching peaks appear at 570/630 nm and 530/580 nm for polymer donors of PM6 and PBTTzE in blend films. Furthermore, the signals at 540, 580 and 740 nm were selected to investigate the decay traces of donors and acceptor, respectively. As shown in Figure 5d, the decay of the BTP-eC9 GSB signals at 740 nm are accompanied with the rise of donors GSB signal at 540 and 580 nm, representing efficient hole transfer. And the signal in the ternary blend decays slightly faster, revealing that the introduction of the third component could form a double transport channel and thus significantly improve the hole transfer from BTP-eC9 to PM6. However, due to the relatively close HOMO energy level, only a small portion of photo-induced band is observed in the binary system of PBTTzE:BTP-eC9 (Figure 5a), which can explain the low PCE in the PBTTzE-based binary device. Further, in Figure 5e, the time constants of decay dynamics were investigated by fitting the GSB signal at 630 nm for PM6 containing blend films and at 590 nm for PBTTzE:BTP-eC9 blend based on the biexponential functions to gain the τ_1 and τ_2, where τ_1 and τ_2 represent the ultrafast exciton dissociation at the interface and the diffusion of the exciton in the domain, respectively. The τ_1/τ_2 are 0.21/12.15 ps, 0.05/6.18 ps, and 0.11/7.72 ps for PBTTzE:BTP-eC9, PM6:BTP-eC9 and PM6:PBTTzE:BTP-eC9, respectively. Obviously, the enhanced τ_1 value could be obtained for the ternary blend, revealing that the possibility of hole transfer process takes advantage of an energy cascade through the PBTTzE. This

Table 3 Photovoltaic parameters of the OSCs for binary and ternary blends

Active layer	V_{oc} [V]	J_{sc} [mA cm^{-2}]	FF	PCE [a] [%]	E_g [eV]	ΔE_1 [eV]	ΔE_2 [eV]	ΔE_3 [eV]	E_{loss} [eV]
PBTTzE:BTP-eC9	0.866	17.86	0.675	10.45 (10.37±0.08)	1.408	0.261	0.059	0.222	0.542
ternary	0.846	28.38	0.782	18.76 (18.62±0.14)	1.414	0.262	0.067	0.238	0.567
PM6:BTP-eC9	0.839	27.01	0.761	17.26 (17.15±0.11)	1.418	0.262	0.077	0.245	0.584

a) Average value was obtained from 15 devices.

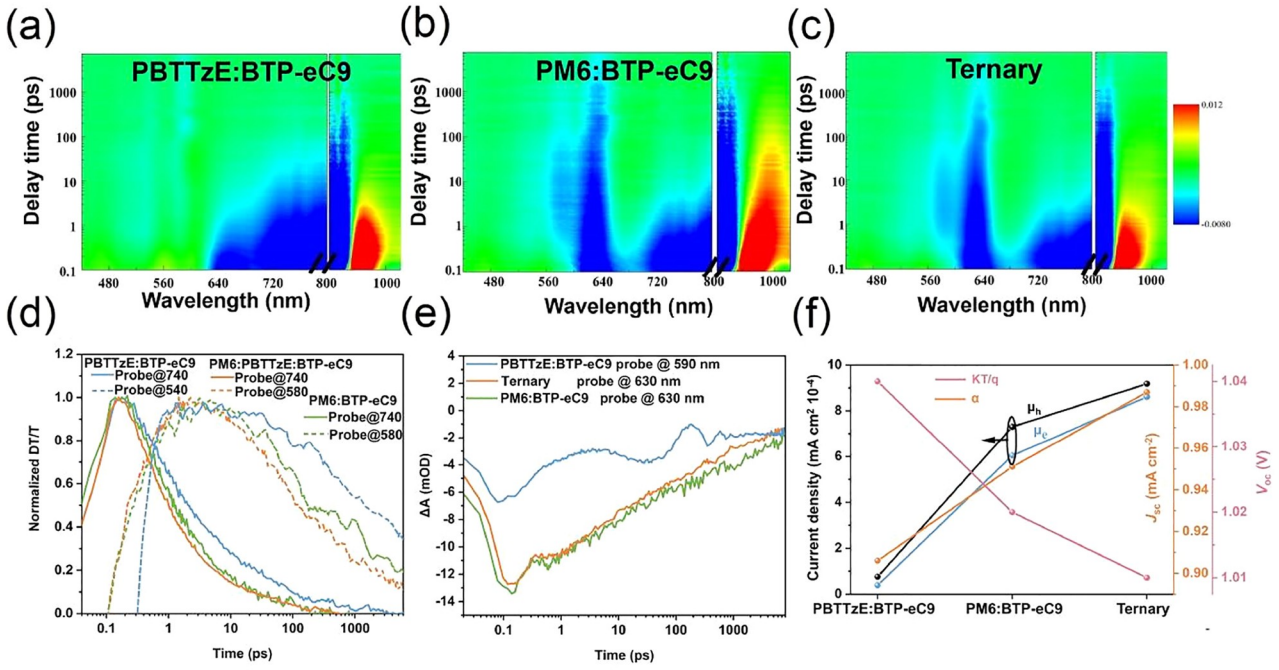

Figure 5 (Color online) (a–c) 2D TAS images of the binary and ternary blend films. (d) The decay traces of donor and acceptor in blend films for PM6:BTP-eC9 and PM6:PBTTzE:BTP-eC9 (probe@580 nm and @740 nm) and PBTTzE:BTP-eC9 (probe@540 nm and @740 nm). (e) Kinetic curves for PM6:BTP-eC9 and PM6:PBTTzE:BTP-eC9 (probe@630 nm) and PBTTzE:BTP-eC9 (probe@590 nm). (f) Mobility, and charge recombination values of the binary and ternary devices.

result also shows that there is no influence on exciton dissociation process when reducing the E_{loss} with ternary strategy. Meanwhile, an improved τ_2 value means an enlarged domain, which is conducive to exciton diffusion to a longer distance within the effective exciton lifetime, thus achieving higher carrier mobility and less charge recombination in the ternary blend. The results were also confirmed by corresponding tests. As shown in Figure 5f, both the α and n values of the optimal ternary OSCs are closer to 1 than those of binary devices. Also, the ternary blend shows the highest hole and electron mobility, and more balanced charge transport mobilities (μ_h/μ_e = 1.07). In addition, the steady state photoluminescence (PL) spectra demonstrate that energy transfer takes place from PBTTzE to PM6 due to the gradually increased intensity in blend films along with PBTTzE content increment as well as partially overlapping between the absorption spectrum of PM6 and PL spectrum of PBTTzE (Figure S23). And the J_{sc} value of the OSC using PBTTzE:PM6 as the active layer is between those of the single component devices based on PBTTzE and PM6, respectively, indicating no significant charge transfer between both donors.

Furthermore, the AFM and TEM were employed to explore the effect of PBTTzE on the surface and bulk morphology of blend films. As presented in Figure S24, the blend film with PBTTzE:BTP-eC9 exhibits an obviously higher RMS roughness of 2.50 nm than 1.81 nm for the PM6-based binary blend film. By incorporating 10 wt% PBTTzE into the PM6:BTP-eC9 blend film, a slightly enhanced RMS value of 2.04 can be observed for ternary blend film with identifiable fiber-like structure (TEM images), indicating improved phase separation. The GIWAXS measurements were carried out as well to study the molecular packing and crystallinity behaviors of the neat polymers and their blend films (Figure 6). Apparent (100) and (010) peaks along OOP direction as well as (100) peak in IP direction can be observed simultaneously, suggesting the coexistence of face-on and edge-on molecular orientation of PM6, similar to the reported result [38]. In contrast, PBTTzE exhibits the preferred face-on orientation due to obvious (100) and (010) peaks along the IP and OOP directions, respectively. Meanwhile, the π-π stacking distance and diffraction intensity are improved in the PBTTzE film with enhanced CCL value. So, when adding PBTTzE into the PM6:BTP-eC9-based binary blend film, the d-spacing value from the 1.69 $Å^{-1}$ changes little, but the corresponding CCL value increases significantly from 19.49 to 20.19 nm (Table S8). It suggests that introduction of PBTTzE as a third component can form more ordered packing and enhanced crystallinity. This feature can facilitate more efficient charge transport, which agrees well with the increased J_{sc} and FF in ternary OSCs. In addition, for the IP lamellar packing peaks, all blend films possess both peaks at ~0.30 $Å^{-1}$ and ~0.40 $Å^{-1}$, which were assigned to the polymers and BTP-eC9, respectively. Moreover, an increased (100) lamellar peak intensity of BTP-eC9 could be observed in PBTTzE:BTP-eC9 blend film, which is probably due to the formation of inferior compatibility between PBTTzE and BTP-eC9 (χ = 0.26) compared to PM6:BTP-eC9 (χ = 0.14) [74]. The large χ value means severe phase separation, which would lead to poor charge transport as well as increased charge recombination, and then explain the reason why PBTTzE:BTP-eC9-based device displays lower J_{sc} and FF.

3 Conclusions

In summary, a simple bithiophene carboxylate-substituted thiazole monomer TTzE-Br was designed and used to construct a series of novel D-A copolymers (PBTTzEs) with

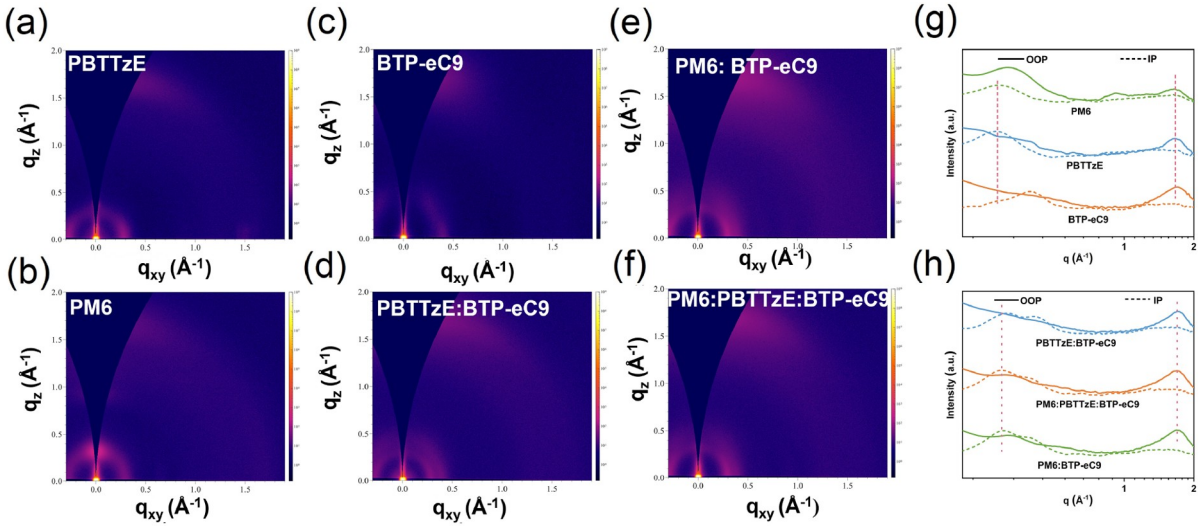

Figure 6 (Color online) (a–f) 2D-GIWAXS patterns of the pristine and blend films; (g–h) Corresponding line-cut profiles in IP and OOP directions.

chlorinated BDT as donor unit by varying the molecular weights. Both D and A units could be synthesized via only three steps, respectively, thus cutting the cost. Interestingly, carboxylate- and chloro-substitution can simultaneously adjust HOMO energy level to ensure a high V_{oc}. Moreover, introduction of the ester group and C=N is helpful for improving the aggregation properties, crystallinity and packing ordering due to the formation of S···O and S···N noncovalent interactions. When paired with IT-4F acceptor, a champion PCE of 15.87% was obtained with moderate molecular weight (54 kDa), representing a record efficiency among the IT-4F-based binary OSCs. Importantly, the PBTTzE exhibited PCE deviation smaller than 1% within a large M_n range of 43–76 kDa, demonstrating superior batch-to-batch reproducibility. Further, PBTTzE was added as a third component to the high performance blend of PM6: BTP-eC9. The calculated χ value confirms that alloyed state could be formed between PM6 and PBTTzE, leading to the enhanced V_{oc} of the ternary device by reducing E_{loss}. In addition, besides the complementary absorption, the optimized BHJ morphology with the improvement of phase separation, crystallinity, and domain size in ternary blend film could be simultaneously regulated by the incorporation of 10 wt% PBTTzE, contributing to increased exciton dissociation, charge transport, thus improved J_{sc} and FF. With all these advantages, the ternary OSCs achieves a high PCE of 18.76% with a simultaneous enhancement of V_{oc}, J_{sc} and FF values in comparison to that of PM6-based binary device. Overall, our results demonstrate that the carboxylate-substituted thiazole is a great potential unit to construct low-cost wide bandgap polymers with deep HOMO energy level for efficient NF-OSCs.

Acknowledgements This work was supported by the National Natural Science Foundation of China (52003209, 51973169, 52273195), Key R & D program of Hubei Province (2022BAA095), Open Key Fund Project of State Key Laboratory of Advanced Technology for Materials Synthesis and Processing of Wuhan University of Technology (2022-KF-34), Scientific Research Foundation of Wuhan Institute of Technology (K202023).

Conflict of interest The authors declare no conflict of interest.

Supporting information The supporting information is available online at http://chem.scichina.com and http://link.springer.com/journal/11426. The supporting materials are published as submitted, without typesetting or editing. The responsibility for scientific accuracy and content remains entirely with the authors.

1 Tang H, Liang Y, Liu C, Hu Z, Deng Y, Guo H, Yu Z, Song A, Zhao H, Zhao D, Zhang Y, Guo X, Pei J, Ma Y, Cao Y, Huang F. *Nature*, 2022, 611: 271–277
2 Lin Y, Li Y, Zhan X. *Chem Soc Rev*, 2012, 41: 4245–4272
3 Shen YF, Zhang H, Zhang J, Tian C, Shi Y, Qiu D, Zhang Z, Lu K, Wei Z. *Adv Mater*, 2023, 35: 2209030
4 Li Z, Wang X, Zheng N, Saparbaev A, Zhang J, Xiao C, Lei S, Zheng X, Zhang M, Li Y, Xiao B, Yang R. *Energy Environ Sci*, 2022, 15: 4338–4348
5 Hu Z, Wang J, Ma X, Gao J, Xu C, Yang K, Wang Z, Zhang J, Zhang F. *Nano Energy*, 2020, 78: 105376
6 Ghezzi D, Antognazza MR, Maccarone R, Bellani S, Lanzarini E, Martino N, Mete M, Pertile G, Bisti S, Lanzani G, Benfenati F. *Nat Photon*, 2013, 7: 400–406
7 Wu Z, Sun C, Dong S, Jiang XF, Wu S, Wu H, Yip HL, Huang F, Cao Y. *J Am Chem Soc*, 2016, 138: 2004–2013
8 Lin Y, Wang J, Zhang ZG, Bai H, Li Y, Zhu D, Zhan X. *Adv Mater*, 2015, 27: 1170–1174
9 Yuan J, Zhang Y, Zhou L, Zhang G, Yip HL, Lau TK, Lu X, Zhu C, Peng H, Johnson PA, Leclerc M, Cao Y, Ulanski J, Li Y, Zou Y. *Joule*, 2019, 3: 1140–1151
10 Pang B, Liao C, Xu X, Yu L, Li R, Peng Q. *Adv Mater*, 2023, 35: 2300631
11 Sun F, Zheng X, Hu T, Wu J, Wan M, Xiao Y, Cong T, Li Y, Xiao B, Shan J, Wang E, Wang X, Yang R. *Energy Environ Sci*, 2024, 17: 1916–1930
12 Chen T, Li S, Li Y, Chen Z, Wu H, Lin Y, Gao Y, Wang M, Ding G, Min J, Ma Z, Zhu H, Zuo L, Chen H. *Adv Mater*, 2023, 35: 2300400
13 Yu X, Ding P, Yang D, Yan P, Wang H, Yang S, Wu J, Wang Z, Sun H, Chen Z, Xie L, Ge Z. *Angew Chem Int Ed*, 2024, 63: e202401518
14 Guo C, Sun Y, Wang L, Liu C, Chen C, Cheng J, Xia W, Gan Z, Zhou J, Chen Z, Zhou J, Liu D, Guo J, Li W, Wang T. *Energy Environ Sci*, 2024, 17: 2492–2499
15 Zhang Y, Deng W, Petoukhoff CE, Xia X, Lang Y, Xia H, Tang H, Chandran HT, Mahadevan S, Liu K, Fong PWK, Luo Y, Wu J, Tsang SW, Laquai F, Wu H, Lu X, Yang Y, Li G. *Joule*, 2024, 8: 509–526
16 Liu K, Jiang Y, Ran G, Liu F, Zhang W, Zhu X. *Joule*, 2024, 8: 835–851
17 Zheng Z, Wang J, Bi P, Ren J, Wang Y, Yang Y, Liu X, Zhang S, Hou J. *Joule*, 2022, 6: 171–184
18 Cui Y, Yao H, Zhang J, Xian K, Zhang T, Hong L, Wang Y, Xu Y, Ma K, An C, He C, Wei Z, Gao F, Hou J. *Adv Mater*, 2020, 32: 1908205
19 Li C, Zhou J, Song J, Xu J, Zhang H, Zhang X, Guo J, Zhu L, Wei D, Han G, Min J, Zhang Y, Xie Z, Yi Y, Yan H, Gao F, Liu F, Sun Y. *Nat Energy*, 2021, 6: 605–613
20 Cao J, Yi L, Zhang L, Zou Y, Ding L. *J Mater Chem A*, 2023, 11: 17–30
21 Li Z, Li X, Xue J, Zhang J, Zhu C, Li J, Ma W, Meng L, Li Y. *ACS Energy Lett*, 2023, 8: 2488–2495
22 Liang Y, Zhang D, Wu Z, Jia T, Lüer L, Tang H, Hong L, Zhang J, Zhang K, Brabec CJ, Li N, Huang F. *Nat Energy*, 2022, 7: 1180–1190
23 Chen S, Hong L, Dong M, Deng W, Shao L, Bai Y, Zhang K, Liu C, Wu H, Huang F. *Angew Chem Int Ed*, 2023, 62: e202213869
24 Luo D, Jiang Z, Tan WL, Zhang L, Li L, Shan C, McNeill CR, Sonar P, Xu B, Kyaw AKK. *Adv Energy Mater*, 2022, 13: 2203402
25 Han Z, Zhang C, He T, Gao J, Hou Y, Gu X, Lv J, Yu N, Qiao J, Wang S, Li C, Zhang J, Wei Z, Peng Q, Tang Z, Hao X, Long G, Cai Y, Zhang X, Huang H. *Angew Chem Int Ed*, 2024, 63: e202318143
26 Qin L, Li X, Dong C, Zhou J, Guo Q, Tang A, Zhong Y, Zhou E. *Chem Eng J*, 2023, 464: 142743
27 Gao J, Zhu X, Bao H, Feng J, Gao X, Liu Z, Ge Z. *Chin Chem Lett*, 2023, 34: 107968
28 Wang J, Luan Q, Wang P, Han C, Bi F, Yang C, Li Y, Bao X. *Adv Funct Mater*, 2023, 33: 2301575
29 Wen TJ, Xiang J, Jain N, Liu ZX, Chen Z, Xia X, Lu X, Zhu H, Gao F, Li CZ. *J Energy Chem*, 2022, 70: 576–582
30 Chen K, Fang H, Zhao C, Fan Q, Ding L, Yan H, Ma W. *Chem Eng J*, 2022, 446: 137375
31 Shen Q, He C, Wu B, Lin Y, Chen S, Gao J, Li S, Ma Z, Ma W, Shi M, Li Y, Chen H. *Chem Eng J*, 2023, 471: 144472
32 Luo D, Brabec CJ, Kyaw AKK. *Nano Energy*, 2023, 114: 108661
33 Li D, Zhang H, Cui X, Chen YN, Wei N, Ran G, Lu H, Chen S, Zhang W, Li C, Liu Y, Liu Y, Bo Z. *Adv Mater*, 2024, 36: 2310362
34 Guo X, Cui C, Zhang M, Huo L, Huang Y, Hou J, Li Y. *Energy Environ Sci*, 2012, 5: 7943–7949

35 Geng Y, Chen Y, Du M, Wu H, Ma Z, Xiao B, Wang H, Tang A, Sun X, Zhong Y, Zhou E. *Adv Energy Mater*, 2024, 14: 2303976
36 Liu C, Shao L, Chen S, Hu Z, Cai H, Huang F. *Prog Polym Sci*, 2023, 143: 101711
37 Qian D, Ye L, Zhang M, Liang Y, Li L, Huang Y, Guo X, Zhang S, Tan Z', Hou J. *Macromolecules*, 2012, 45: 9611–9617
38 Zhang M, Guo X, Ma W, Ade H, Hou J. *Adv Mater*, 2015, 27: 4655–4660
39 Liu Q, Jiang Y, Jin K, Qin J, Xu J, Li W, Xiong J, Liu J, Xiao Z, Sun K, Yang S, Zhang X, Ding L. *Sci Bull*, 2020, 65: 272–275
40 Bin H, Zhang ZG, Gao L, Chen S, Zhong L, Xue L, Yang C, Li Y. *J Am Chem Soc*, 2016, 138: 4657–4664
41 Xu J, Feng H, Liang Y, Tang H, Tang Y, Du Z, Hu Z, Huang F, Cao Y. *J Energy Chem*, 2022, 66: 382–389
42 Luo Y, Chen X, Xiao Z, Liu S, Yin M, Ding L. *Mater Chem Front*, 2021, 5: 6139–6144
43 Sun C, Pan F, Bin H, Zhang J, Xue L, Qiu B, Wei Z, Zhang ZG, Li Y. *Nat Commun*, 2018, 9: 743
44 Yuan X, Zhao Y, Zhan T, Oh J, Zhou J, Li J, Wang X, Wang Z, Pang S, Cai P, Yang C, He Z, Xie Z, Duan C, Huang F, Cao Y. *Energy Environ Sci*, 2021, 14: 5530–5540
45 Shao Y, Gao Y, Sun R, Zhang M, Min J. *Adv Mater*, 2023, 35: 2208750
46 Zhang T, An C, Cui Y, Zhang J, Bi P, Yang C, Zhang S, Hou J. *Adv Mater*, 2022, 34: 2105803
47 Wu X, Zhang X, Zhang J, Wu Y, Li J, Kong X, Li Z, Zhang X, Li X, Li A, Yang G, Sun C. *Adv Funct Mater*, 2024, 2405168
48 Wang X, Zhao R, Ding Z, Liu SF, Li Y. *Sci China Chem*, 2022, 65: 1775–1781
49 Li Z, Zhong W, Ying L, Liu F, Li N, Huang F, Cao Y. *Nano Energy*, 2019, 64: 103931
50 Schopp N, Sabury S, Chaney T, Zhang J, Wakidi H, Kim BM, Sankar R, Luong HM, Therdkatanyuphong P, Brus VV, Marder S, Toney MF, Reynolds JR, Nguyen TQ. *ACS Energy Lett*, 2023, 8: 3307–3313
51 Hoefler SF, Rath T, Pastukhova N, Pavlica E, Scheunemann D, Wilken S, Kunert B, Resel R, Hobisch M, Xiao S, Bratina G, Trimmel G. *J Mater Chem A*, 2018, 6: 9506–9516
52 Xu M, Zhang D, Wang Z, Liu Z, Gao X, He J, Gao Y, Li Z, Shao M. *Chem Eng J*, 2022, 440: 135829
53 Wang W, Wu Q, Sun R, Guo J, Wu Y, Shi M, Yang W, Li H, Min J. *Joule*, 2020, 4: 1070–1086
54 Zhao T, Wang H, Pu M, Lai H, Chen H, Zhu Y, Zheng N, He F. *Chin J Chem*, 2021, 39: 1651–1658
55 An C, Hou J. *Acc Mater Res*, 2022, 3: 540–551
56 Wang X, Li Z, Zheng X, Xiao C, Hu T, Liao Y, Yang R. *Adv Funct Mater*, 2023, 33: 2300323
57 Ma R, Liu T, Luo Z, Guo Q, Xiao Y, Chen Y, Li X, Luo S, Lu X, Zhang M, Li Y, Yan H. *Sci China Chem*, 2020, 63: 325–330
58 Xue C, Tang Y, Liu S, Feng H, Li S, Xia D. *New J Chem*, 2020, 44: 13100–13107
59 Min J, Luponosov YN, Cui C, Kan B, Chen H, Wan X, Chen Y, Ponomarenko SA, Li Y, Brabec CJ. *Adv Energy Mater*, 2017, 7: 1700465
60 Xiao J, Jia X, Duan C, Huang F, Yip HL, Cao Y. *Adv Mater*, 2021, 33: 2008158
61 Gao X, Jing W, Wang Y, Xu X Zhang L, Chen Z, Wen J, Gao J, Peng Q, Liu Z. *Sci. China Mater.*, 2023, 66, 2159–2168
62 Deng J, Huang S, Liu J, Zhou D, Zhao L, Liu L, Huang B, Cheng Y, Yang C, Wu F, Chen L. *Chem Eng J*, 2022, 443: 136515
63 Wu J, Fan Q, Xiong M, Wang Q, Chen K, Liu H, Gao M, Ye L, Guo X, Fang J, Guo Q, Su W, Ma Z, Tang Z, Wang E, Ade H, Zhang M. *Nano Energy*, 2021, 82: 105679
64 Zhang S, Qin Y, Zhu J, Hou J. *Adv Mater*, 2018, 30: 1800868
65 Zhang T, An C, Bi P, Lv Q, Qin J, Hong L, Cui Y, Zhang S, Hou J. *Adv Energy Mater*, 2021, 11: 2101705
66 Gayathri RD, Gokulnath T, Park HY, Kim J, Kim H, Kim J, Kim BS, Lee Y, Yoon J, Jin SH. *ACS Appl Mater Interfaces*, 2022, 14: 10616–10626
67 Wang K, Li W, Guo X, Zhu Q, Fan Q, Guo Q, Ma W, Zhang M. *Chem Mater*, 2021, 33: 5981–5990
68 Jung H, Yu G, Kim J, Bae H, Kim M, Kim K, Kim BS, Lee Y. *Sol RRL*, 2021, 5: 2100513
69 Guo H, Zhang Y, Chen L, Liao X, Xie Q, Cui Y, Huang B, Yang C, Chen Y. *J Mater Chem A*, 2019, 7: 27394–27402
70 Ma P, Wen S, Wang C, Guo W, Shen L, Dong W, Lu J, Ruan S. *J Phys Chem C*, 2016, 120: 19513–19520
71 Chen H, Miao J, Yan J, He Z, Wu H. *IEEE J Sel Top Quantum Electron*, 2016, 22: 66–72
72 Peng W, Lin Y, Jeong SY, Firdaus Y, Genene Z, Nikitaras A, Tsetseris L, Woo HY, Zhu W, Anthopoulos TD, Wang E. *Chem Mater*, 2021, 33: 7254–7262
73 Zhan L, Li S, Li Y, Sun R, Min J, Chen Y, Fang J, Ma CQ, Zhou G, Zhu H, Zuo L, Qiu H, Yin S, Chen H. *Adv Energy Mater*, 2022, 12: 2201076
74 Xu C, Ma X, Zhao Z, Jiang M, Hu Z, Gao J, Deng Z, Zhou Z, An Q, Zhang J, Zhang F. *Sol RRL*, 2021, 5: 2100175